EXPERIMENTAL RESEARCH FOR AERODYNAMIC INTERFERENCE BY UPPER MOUNTED ENGINE EXHAUST JET ON SST CONFIGURATIONS

Dong-Youn KWAK*, Tomonari HIROTANI*, Masayoshi NOGUCHI*, Takeshi ITO*
***Japan Aerospace Exploration Agency**

Keywords: *SST, Wind tunnel test, Aerodynamics, Engine exhaust*

Abstract

Low speed wind tunnel tests were conducted to understand the aerodynamic interferences caused by the engine exhaust jet on an SST configuration where the engine nacelle mounted over the fuselage. High pressure air was exhausted from the nozzle installed inside of the nacelle to simulate the engine exhaust jet flow. The effects of the jet exhaust by the jet strength, model attitude, and tail geometries were investigated. The interferences caused by the jet exhaust were depended on the NPR and freestream velocity. The aerodynamic effects by the jet exhaust were influenced by the angles of attack and the deflection angles of the horizontal tails.

1 Introduction

Japan Aerospace Exploration Agency (JAXA) has performed the research and development programs for the supersonic transport (SST) since 1997 [1]. The low drag aerodynamic design technology was established by the NEXST program (1997-2007) [2-4]. The "Silent Supersonic Technology Demonstration (S3TD) Program" has conducted since 2006 [5]. The demonstration of the low sonic boom design technology is one of the main objectives in this program.

Figure 1 shows a schematic of the 2nd configuration of the S3TD. The engine nacelle is mounted over the rear fuselage. The concept of the upper mounted engine nacelle configurations for the high speed commercial aircrafts was conceived for the environmental aspects. The jet exhaust noise at the take-off and landing flights will be reduced by the shielding

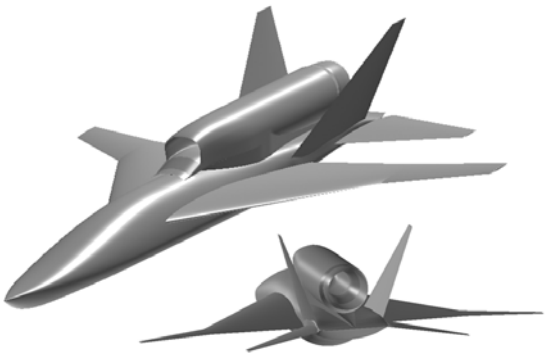

Fig.1 Schematics of the 2nd configuration of S3TD

using the vertical tails and fuselage. In addition, the low sonic boom design of the rear fuselage and tails becomes simple, because strong boom wave generated from the engine nacelle propagates to upside of the aircraft. Therefore, the aircraft designer can focus on the rear parts geometries for the boom reduction.

In this configuration, it is assumed that the aerodynamics is strongly influenced by the engine exhaust jets and engine intake flow. Especially, strong interference will be generated from the flow fields at high alpha and low speed flight conditions such as the take-off and landing. Therefore, the understanding and predicting of the aerodynamic interference are very important on the design process. However, experimental data to validate of the prediction results analyzed by CFD were not so much, because much cost was required for the wind tunnel tests.

The interferences by the engine exhaust jets at the take-off and landing flight conditions were focused on the first step of these issues. In this research, the low speed wind tunnel tests were conducted on a model where the engine exhaust was simulated. The objectives of this

research are (1) to establish the techniques of the wind tunnel test, (2) to understand the aerodynamic interference, and (3) to obtain the aerodynamic data to develop a CFD prediction tool. The first objective was already validated in reference 6. The second objective is discussed in this paper.

2 Experimental Set-ups

2.1 SST Model

The wind tunnel test model was manufactured as a 12% scale of the 2nd S3TD. And the engine intake geometry was modified for the wind tunnel tests (Fig.2). The overall size of the model was decided by the diameter of the engine nozzle. The nozzle diameter was determined from the capability of the exhaust jets using the high pressure air supply system in JAXA. The wind tunnel model was composed of two parts. One of both was the main part that was composed of the forward fuselage, main wing, and engine nozzle. The other was the rear part including the rear fuselage, tail wings, and engine nacelle. The rear part was mechanically separated from the main part. Only internal balance connected the main part to the rear parts. Thus, aerodynamic forces acting on the rear part were measured by the six component internal balance. 50 points of surface static pressures at the main part and rear part were measured by the electronic pressure scanning system (PSI) which located at the inside of the forward fuselage. To minimize the interference by the pressure tubing, the calibration of the internal balance was conducted using the wind tunnel test model configuration.

2.2 Wind Tunnel Test

The wind tunnel tests were conducted in a JAXA 6.5×5.5m low-speed wind tunnel (Fig.3). Figure 4 shows the overall layout of the wind tunnel tests. High pressure air was supplied from the outside of the test section, and was controlled by the mass flow control system. Then the controlled flow was exhausted from the model engine nozzle to the freestream through the flexible pipes and model supporting

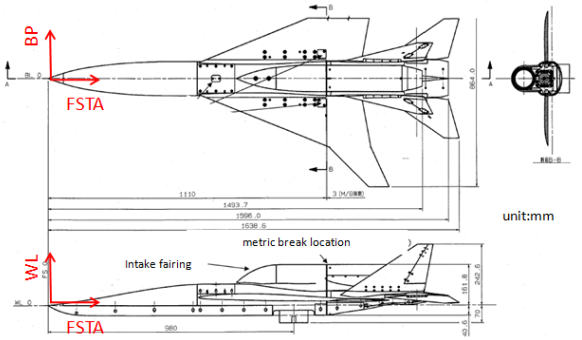

Fig.2 Schematics of the wind tunnel test model

Fig.3 Photos of the wind tunnel tests (JAXA-LWT1)

system. The jet exhaust effects were simulated by control of the mass flow. The strength of the exhaust jet is determined by the ratio of total pressure at the nozzle exit to the freestream static pressure (the nozzle pressure ratio: *NPR*). The *NPR* meant the jet expansion at the downstream flow field of the nozzle. The relation of the mass flow and the *NPR* were obtained by the bench tests using the mass flow control system and the jet engine nozzle. Therefore, the *NPR* can be set to an arbitrary value by controlling the mass flow. At the low speed wind tunnel tests, the *NPR*=1.0 was nearly equaled to the condition of no exhaust. The total pressure, temperature, and static

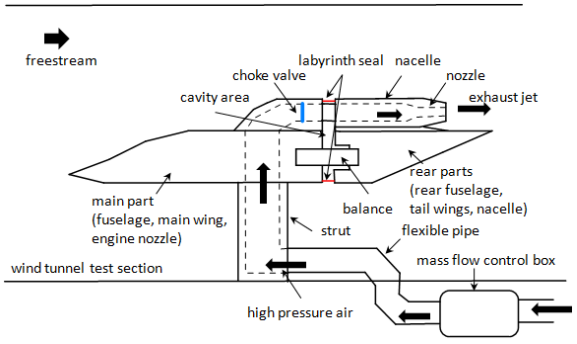

Fig.4 Overall layout of the wind tunnel tests

pressure near the exit of the nozzle station were measured to cross-check the *NPR* values. The aerodynamic measurements were conducted at the several *NPR* for each model attitude.

The wind tunnel tests were mainly performed in U=50m/s of the freestream velocity. However, the aerodynamic forces at several freestream velocities were also measured to understand the Reynolds number effects. The Reynolds number based on the mean aerodynamic chord length was Re=1.7×10^6 (U=50m/s). The *NPR* was changed on the range of *NPR*=1.0–2.23. The required maximum *NPR* for the take-off is 2.9 that determined by the maximum power lever angle. Aerodynamic coefficients (C_L, C_D, C_m, etc.) were normalized using the main wing area and the mean aerodynamic chord length of the main wing (*MAC*). The C_m was determined by the pitching moment component around the 25% *MAC* station.

2.3 Data Processing

The data processing and correction were performed to improve the accuracy of the measured aerodynamic data. As shown in figure 2 and figure 4, the rear part of the wind tunnel test model was mechanically separated from the main part. Therefore, the cavity area between the main part and rear part was sealed by the labyrinth seals to minimize the flow interferences. The pressure measurement was conducted at 12 points of the cavity area to correct the measured aerodynamic forces acting on the rear part. The influence by the cavity area mainly affects to an axial force component.

An influence of the model strut to the flow field was one of the serious problems in this wind tunnel test configurations (see Fig. 3). The model strut in this test was thicker than the conventional strut, because high pressure air was supplied through the inside of the strut. Therefore, flow field behind the strut was strongly influenced by the strut. Figure 5 (a) compares the surface static pressure distribution C_p obtained by the wind tunnel test and CFD analysis. Relatively good agreement of both results was observed at the upper surface of the wing, whereas large difference was indicated at

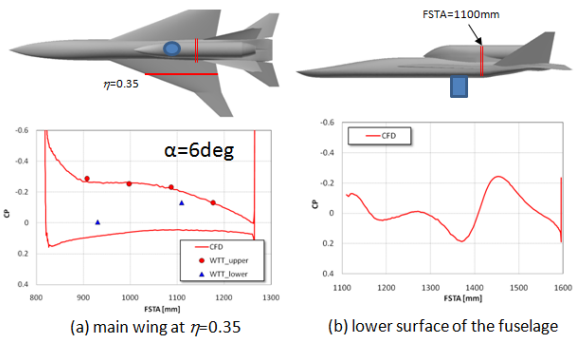

Fig.5 Interference by the model strut(α=6deg,U=50m/s)

the C_p distributions of the lower surface. Those differences were caused by accelerated flow around the strut in the wind tunnel tests. It means that aerodynamic forces measured by the internal balance involve the strut interferences. Thus, the wind tunnel test results were corrected using the pressure distributions at the lower surface of the rear fuselage which derived by the CFD analysis (Figure 5 (b)).

3 Results and Discussion

3.1 Effects of the Exhaust Jet

Figure 6 shows the aerodynamic forces acting on the rear parts of a baseline configuration at α=2deg (the vertical tail: nominal location, the deflection angles of the horizontal tail: δ_{HT}=0deg). By increasing the *NPR* from 1.0 to 1.4, the C_L, C_D and pitch-down moment nonlinearly increase, whereas each coefficient keep a constant value at the range of the *NPR*=1.4 – 2.1. Figure 7 and 8 show the C_P

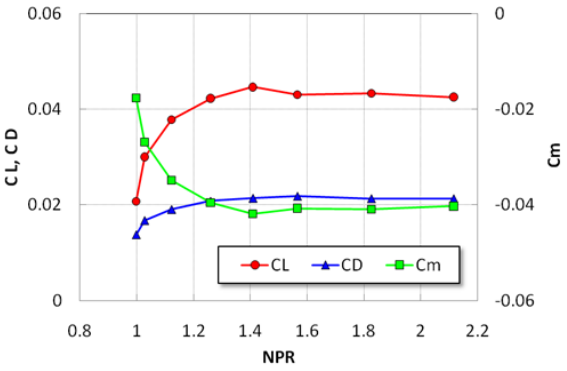

Fig.6 Aerodynamic force characteristics by the exhaust effects for the baseline configuration (α=2deg, U=50m/s)

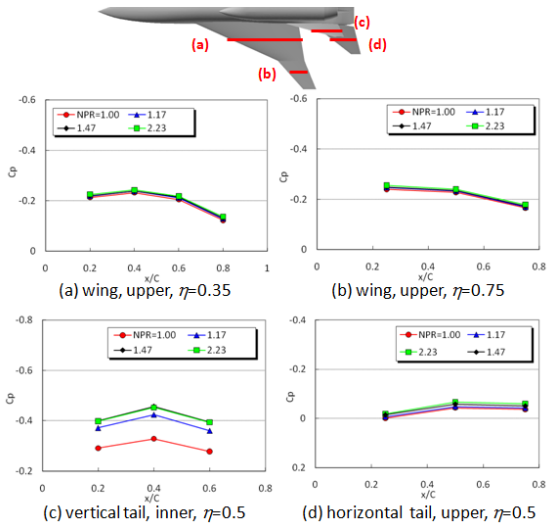

Fig.7 C_p distributions at several locations of the baseline configuration (α=2deg, U=50m/s)

distributions at several stations of the model. With increasing the *NPR*, no obvious change of the C_P were observed at the main wing (Fig 7 (a), (b)), whereas large increment of the suction was observed at the inner surface of the vertical tail (Fig. 7 (c)). Large changes of the C_P were also appeared around the engine nacelle (Fig. 8 (a), (b)). Compare with both C_P distributions which measured at different *x*-stations ((a): FSTA =1265mm, (b): FSTA =1397mm) around the nacelle, the C_P distribution in the (b) that located closer to the nozzle (FSTA=1494mm) than the (a) shows the large increment of suction than the C_P in the (a). Similar trend was observed at the C_P distributions of the upper surface of the rear fuselage. The C_P at FSTA=1494mm (Fig.8 (c)) had larger change than the C_P at FSTA=1540mm (Fig.8 (d)). It meant that some areas that located near the engine nozzle were strongly influenced by the exhaust jet. Figure 8 (e) shows the C_P distributions along the FSTA at a buttock plane (BP=49mm) between the nacelle and vertical tail. Large increments of the C_P were obtained at FSTA=1331mm and FSTA=1397mm in which area was blocked by the vertical tail. The flows through the area which was blocked by the nacelle and vertical tail were significantly accelerated by the exhaust jet, and then induced the increment of the suction pressure. The flow fields near the engine nozzle were influenced by the exhaust jet. Those effects caused the increment of the C_L, C_D and the pitch-down C_m.

Figure 9 shows the exhaust jet effects at the different freestream velocities. Although the shapes of the C_L curves at the different *NPR* are similar, the change of the C_L on U=30m/s is the largest among the other cases. The C_D and C_m curves (Fig. 9 (b), (c)) indicated the same results of the C_L curves. The increments of the aerodynamic forces by the exhaust effect strongly depended on the freestream velocity although those had same values of the *NPR*. Figure 10 shows the changes of the C_P distributions (ΔC_P) at some locations where large changes by the exhaust jet were obtained in figure 7, 8. The trend of the C_P distribution variation at several freestream velocities was similar to the aerodynamic force characteristics shown in figure 9. Figure 11 shows the ΔC_P at

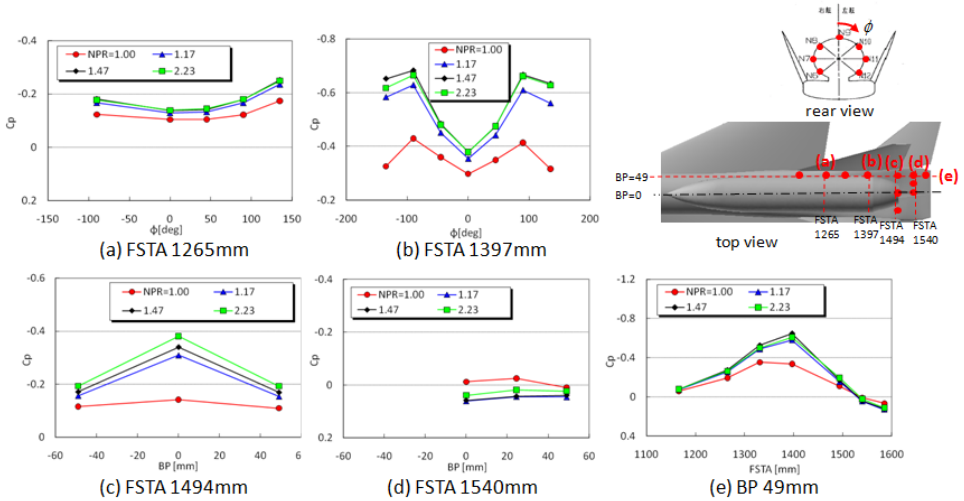

Fig.8 C_p distributions at the tails of the baseline configuration (α=2deg, U=50m/s)

each location as variation of a thrust coefficient (C_j) and freestream velocity. The thrust coefficient was determined by Eq. 1.

$$C_j = \frac{q_j S_j}{q S} \qquad (1)$$

Where, q_j is a dynamic pressure of exhaust jet at the engine nozzle, and S_j is a cross section area of the nozzle. The q and S are the freestream dynamic pressure and the wing area. The ΔC_P at each location were linearly changed to the $C_j{*}U/U_{max}$ (U_{max} is a reference value to normalize the freestream velocity; U_{max}= 60m/s). In addition, the ΔC_P became to zero at $C_j{*}U/U_{max}$ = 0. It was cleared that the effects by the jet exhaust were depended on the *NPR* and freestream velocity.

3.2 Model attitude

Figure 12 shows the C_L, C_D and C_m curves for the baseline configuration by the exhaust jet at several angles of attack. The effects of the exhaust jet at several angles of attack are indicated with the similar results on α=2deg (see Fig. 6). Figure 13 shows the difference of the aerodynamic forces on the *NPR*=1.0 and the *NPR*=2.2 (ΔC_L, ΔC_D ΔC_m). With increasing angle of attack, the ΔC_L and ΔC_D slightly increase and the ΔC_m decreases. Figure 14 shows the overall aerodynamic forces (C_{Lt}, C_{Dt} C_{mt}) measured by another wind tunnel tests (a JAXA 2m x 2m low-speed wind tunnel). The overall aerodynamic forces without the jet effects included the forces acting on the main part and rear part (the red curves). The overall aerodynamic forces including the jet effects (the blue curves) were estimated by adding the jet effects obtained in this research to the red curves. Figure 14 clearly indicates the jet effect versus the overall aerodynamic forces. The C_{Lt}-C_{Dt} curve including the exhaust jet effect was slightly different from the curve without the jet effect (Fig. 14 (d)). Minimum C_{Dt} ($C_{Dmin\ t}$) of the jet-on case is larger than the C_{Dmin} of the jet-off case. The pitch-down moment at a same C_{Lt} at the jet-on case is slightly larger than that at the jet-off case.

Figure 15 shows the aerodynamic forces at the different side-slip angles. The longitudinal

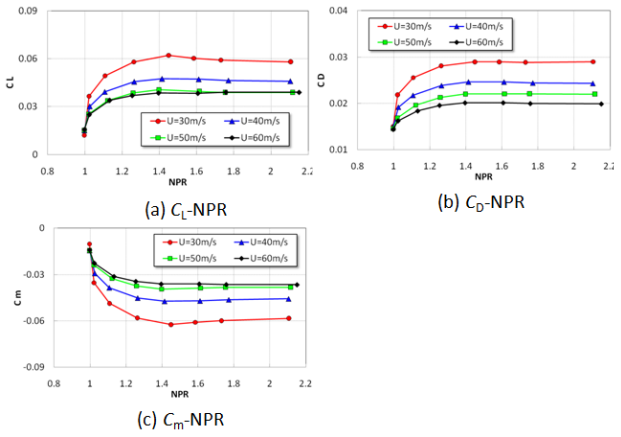

Fig.9 Effects of the freestream velocities (α=2deg)

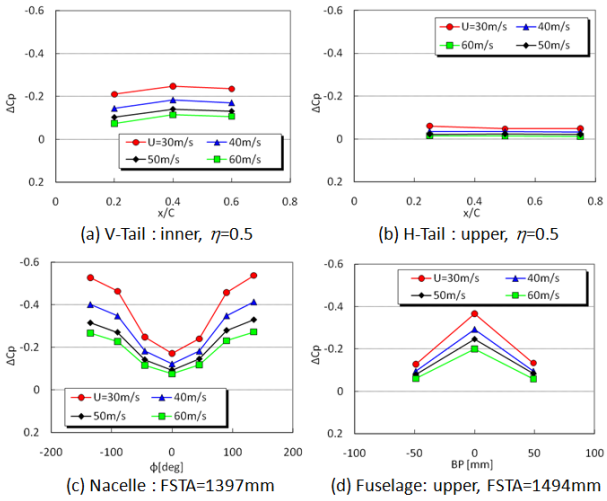

Fig.10 ΔC_p distributions at the different freestream velocities (α=2deg)

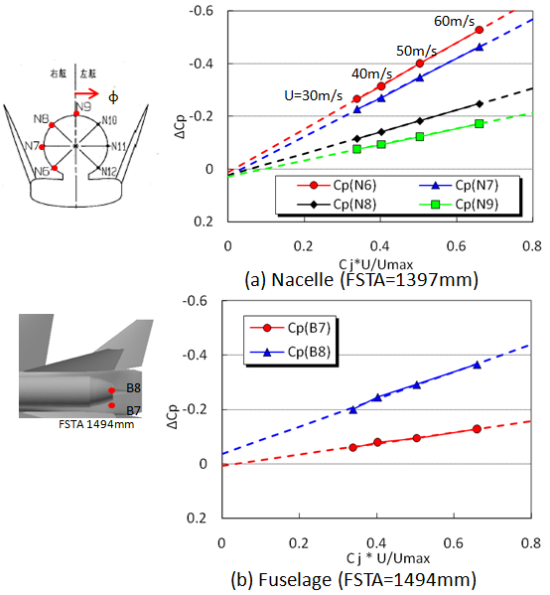

Fig.11 ΔC_p characteristics by the jet thrust coefficient and the freestream velocities (α=2deg)

aerodynamic forces (C_L, C_D, C_m) indicated the

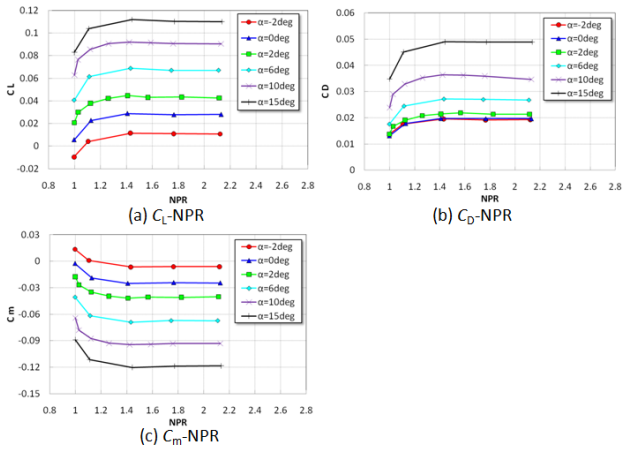

Fig.12 Effects of the angles of attack

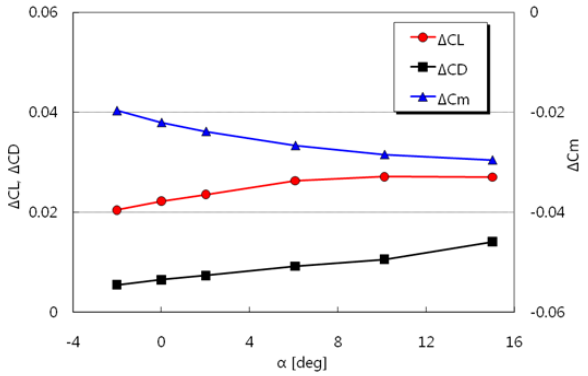

Fig.13 The changes of the aerodynamic forces by the exhaust effects

significant exhaust effects, whereas no obvious changes of the exhaust effects were observed on the lateral aerodynamic forces (C_Y, C_l, C_n). The similar trend was observed for three cases which have the different side-slip angles. The effects of the jet exhaust did not depend on the side-slip angles, although the effects depended on the angles of attack.

3.3 Tail Geometries

3.3.1 Vertical and Horizontal Tails

The jet exhaust effects by the vertical tails and horizontal tails were investigated. Figure 16 shows the change of the aerodynamic forces (ΔC_L, ΔC_D ΔC_m) by the jet exhaust effects for three configurations. Each aerodynamic force was derived by the difference of the force on the *NPR*=1.0 and the *NPR*=2.2 for each configuration. The green curves corresponded to the jet exhaust effects induced by the tail configuration without the vertical and horizontal tails. A difference of the green curves and the blue curves means the effects caused by the horizontal tails. Furthermore, a difference of the blue and the red means the effects caused by the vertical tails. The differences of the blue curves and the red curves are larger than the difference of the green and the blue. It meant that the vertical tails induced strong effects of the jet exhaust. The effects by the horizontal tails were smaller than the vertical tail effects because the horizontal tails located far than the vertical tails from the engine nozzle. In addition, no change by the horizontal tails was obtained on the ΔC_D.

Figure 17 shows the ΔC_P distributions induced by the jet exhaust for each configuration. As same manner with figure 16, the ΔC_P distributions were derived by the difference of the C_P on the *NPR*=1.0 and

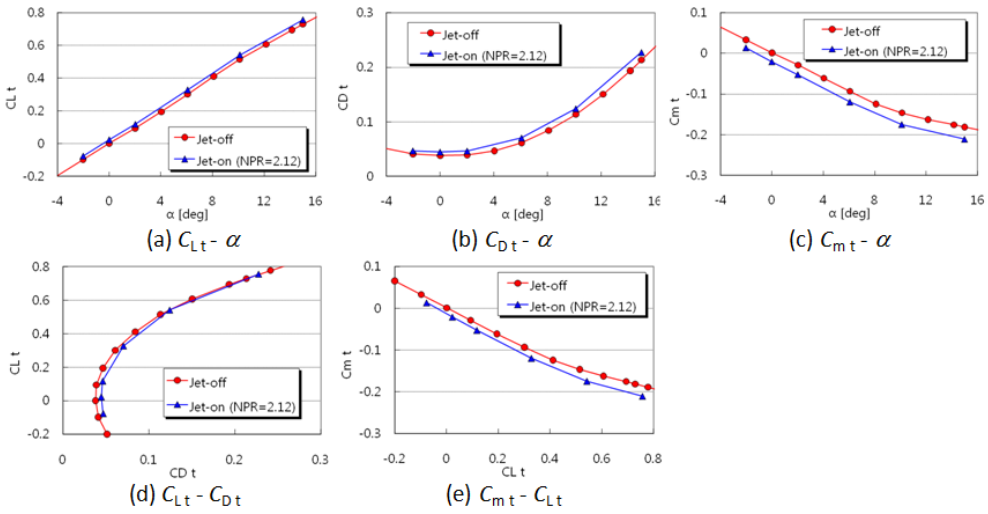

Fig.14 Effects of the jet exhaust on the overall aerodynamic forces

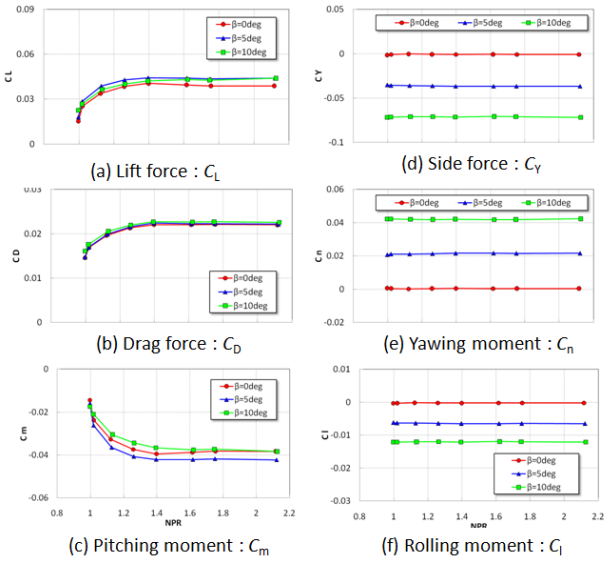

Fig.15 Effects of the side-slip angles (α=2deg)

NPR=2.23. The jet exhaust effects indicated that the C_P distributions (Fig.17) corresponded with the aerodynamic forces results (Fig.16). The largest effects of the jet exhaust were obtained for the baseline configurations. It meant that the effects of the jet exhaust caused by the vertical tails were stronger than the other parts. Induced

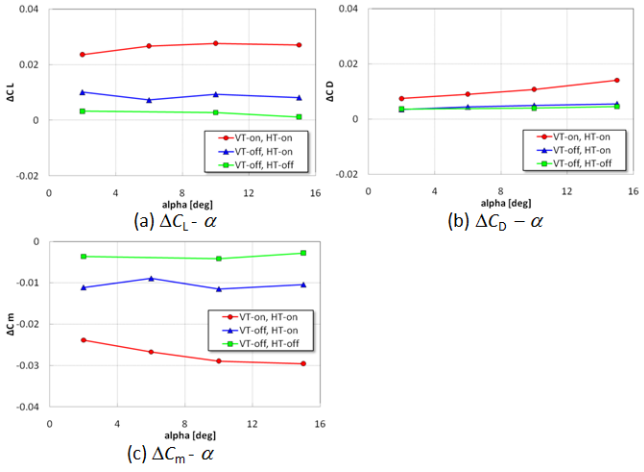

Fig.16 Effects by the vertical tails and the horizontal tails

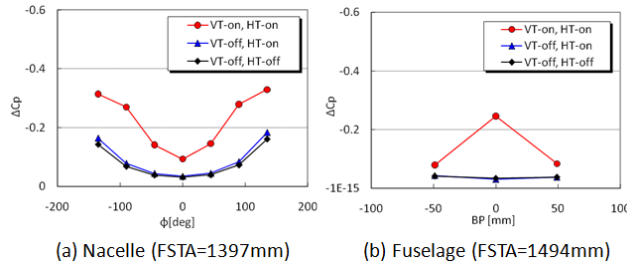

Fig.17 ΔC_p distributions by the vertical tails and the horizontal tails (α=10deg)

effects by the vertical tails were composed of two components. One component was the effect that directly acted to the vertical tails (see Fig. 7(c)). The other was the increment of the suction force caused by the vertical tails at the nacelle and fuselage. Thus, the ΔC_P distributions shown in figure 17 indicated the larger increments at the nacelle and fuselage. The effects by the horizontal tails were smaller than the effects by the vertical tail.

3.3.2 Vertical Tail Locations

Figure 18 shows the effects by the jet exhaust at the difference of the vertical tail locations. Compared with the nominal location of the vertical tail (the baseline), the vertical tail location moved 36mm to the rearward direction, and or moved 12mm to the inward direction. The differences of the aerodynamic force of the *NPR*=1.0 and the *NPR*=2.2 are shown in figure 18. Similar changes were observed on three curves. It meant that the locations of the vertical tail tested in this research did not induce significant change of the jet exhaust effects.

3.3.3 Deflection Angles of Horizontal Tail

The jet exhaust effects at the different

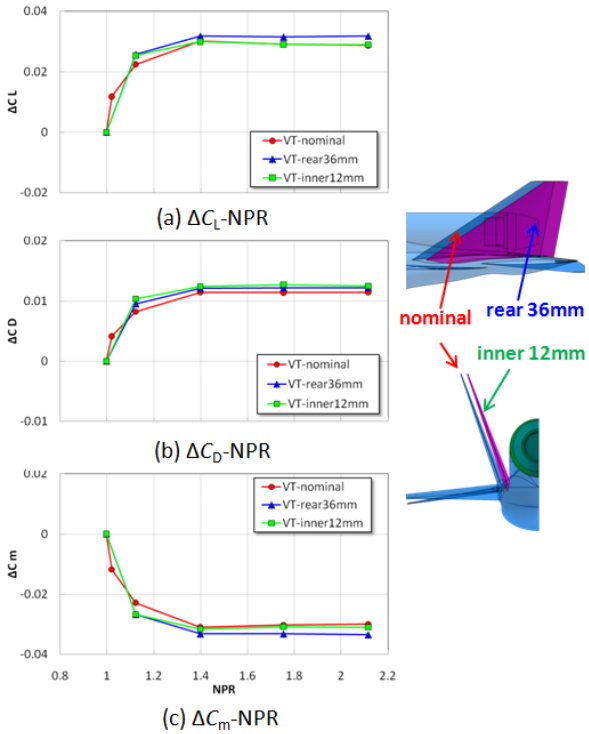

Fig.18 Exhaust effects by the location of the vertical tails (α=10deg)

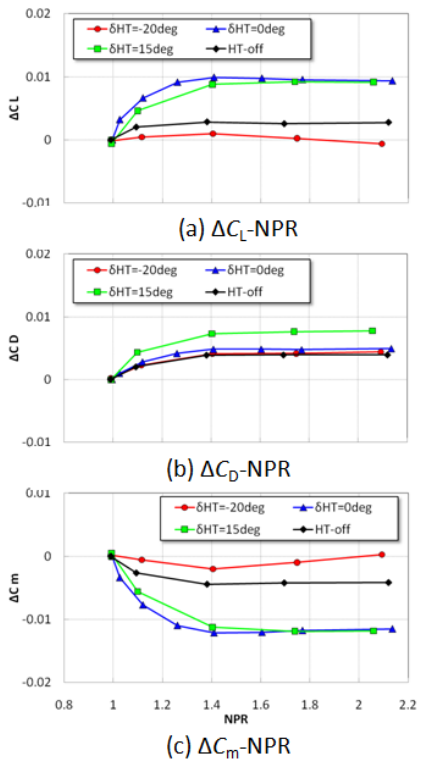

Fig.19 Exhaust effects by the deflection angles of the horizontal tail (α=10deg)

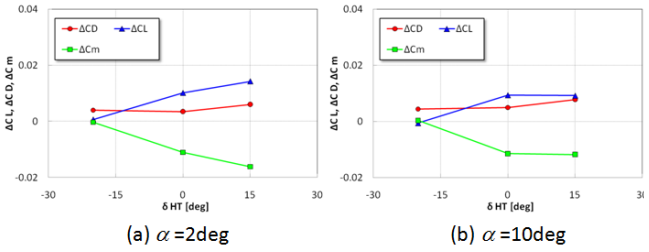

Fig.20 Aerodynamic force characteristics at the different deflection angles of the horizontal tail

deflection angles of the horizontal tail were investigated. All configurations shown in this section (Fig.19, 20, 21) had no vertical tails. Therefore, it was supposed that the effects by the horizontal tails for the configurations without the vertical tails were larger than the effects for the baseline configuration (with the vertical tail), because the vertical tails reduced the effects acted on the horizontal tails by geometrically blocking the exhaust effects. However, it was thought that a qualitative trend by the deflection angles of the horizontal tail could be discussed in these configurations.

Figure 19 shows the aerodynamic force at the several deflection angles of the horizontal tail. Each force was obtained from the difference of the aerodynamic forces of several *NPR* and the *NPR*=1.0. Therefore, the C_L, C_D, C_m had zero at the *NPR*=1.0. The jet exhaust effects were strongly influenced by the deflection angles of the horizontal tail (δ_{HT}). The largest increments of the C_L by the exhaust effects were observed in the cases of δ_{HT}=0deg, 15deg. Smaller change of the C_L was observed at δ_{HT}=-20deg. That was slightly larger than the result of the no tails. The similar trend was also observed on the C_m characteristics, whereas the C_D for the δ_{HT}=15deg configuration indicated the larger change of the exhaust effects than the other three configurations. Figure 20 shows the difference of the aerodynamic force caused by the jet exhaust that obtained from the results at the *NPR*=2.2 and *NPR*=1.0. It was cleared that effects of the jet exhaust increased by increasing the deflection angles of the horizontal tail from δ_{HT}=-20deg to δ_{HT}=15deg. Figure 21 shows the ΔC_P distributions at the different deflection angles of the horizontal tail. Large increment of the C_P suction was observed at the upper surface of the horizontal tail for δ_{HT}=15deg (Fig. 21 (a)). Especially, significant suction increment was obtained at aft part of the horizontal tail (x/C_r =0.5, 0.75) although the rear part of the horizontal tail located far away from the nozzle

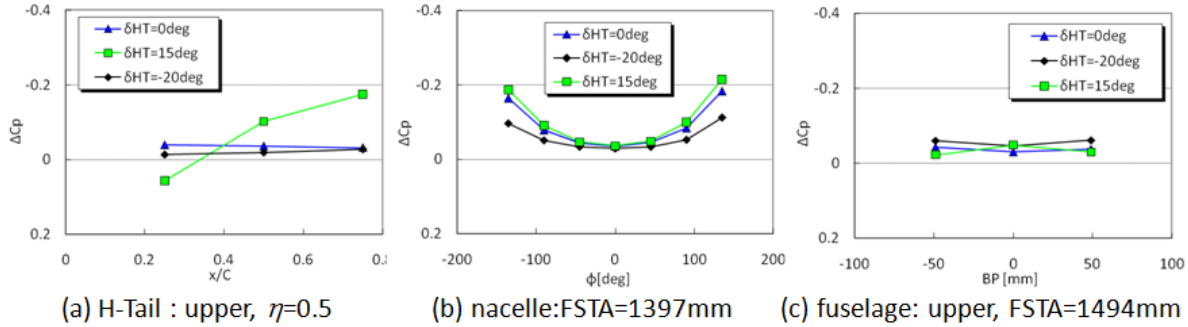

Fig.21 ΔC_p distributions at the different deflection angles of the horizontal tails (α=10deg)

than those at the δ_{HT}=0 and δ_{HT}=-20deg. It was suggested that the flow field at the rear part of the horizontal tail that had δ_{HT}=15deg was strongly influenced by the jet exhaust flow. The induced flow by the jet exhaust contributes to prevent the flow separation at the horizontal tail. The large increments of the C_P suction were obtained at FSTA=1494mm for δ_{HT} =0deg and 15deg. The trend of the C_P characteristics in figure 21 (b) was agreement with the aerodynamic force results shown in figure 19 and 20. The effects by the jet exhaust were strongly influenced by the deflection angles of the horizontal tail.

4 Conclusions

The low speed wind tunnel tests were conducted to understand the aerodynamic interactions by the engine exhaust jet. High pressure air was exhausted from the nozzle mounted on the upper fuselage to simulate the engine exhaust jet effect. The effects of the jet exhaust by the strength of the exhaust jet, model attitude, and tails geometries were investigated.

- With increasing the *NPR*, nonlinear increment of the C_L, C_D, and C_m were observed at *NPR*=1.0 – 1.4, whereas the aerodynamic forces kept a constant value at *NPR*=1.4-2.2.
- The jet exhaust effects depended on the freestream velocity.
- The change of the aerodynamic forces (ΔC_L, ΔC_D ΔC_m) by the exhaust effects were slightly increased when the angles of attack increased. However, no obvious change of the jet exhaust effects was observed at several side-slip angles.
- The locations of the vertical tails within a 36mm to the rearward direction or a 12mm to the inward direction did not influence the jet exhaust effects.
- The effects by the jet exhaust were strongly influenced by the deflection angles of the horizontal tail.

Acknowledgements

This research was able to be performed by the helpful support of many researchers. Authors wish to thank the low speed wind tunnel group for their help in support of the wind tunnel tests.

References

[1] Ohnuki, T., Hirako, K., Sakata, K., ”National Experimental Supersonic Transport Project”, ICAS-2006-1.4.1.

[2] Yoshida, K., “Supersonic drag reduction technology in the scaled supersonic experimental airplane project by JAXA”, *Progress in Aerospace Sciences*, Vol. 45, pp 124-146, 2009.

[3] Kwak, D.Y., Tokugawa, N., Yoshida, K, “Demonstration of Aerodynamic Design Technologies on Supersonic Experimental Airplane (NEXST-1) by Flight Test”, *Proceedings of 2006 KSAS-JSASS Joint International Symposium on Aerospace Engineering*, 2006, pp.176-182, 2006.

[4] Tokugawa, N., Kwak, D.Y., Yoshida, K. and Ueda, Y, “Transition Measurement of Natural Laminar Flow Wing on Supersonic Experimental Airplane (NEXST-1)”, Jour. of Aircraft, Vol.45, No.5, pp1495-1504, 2008.

[5] Murakami, A., “Silent Supersonic Technology Demonstrator Program”, ICAS-2006-1.4.2.

[6] Hirotani, T., Kwak, D.Y., Noguchi, M. And Ito, T.,”Low-Speed Wind Tunnel Tests on the Silent Supersonic Technology Demonstrator Model using Cold Simulant Exhaust Gas”, JSASS Annual Meeting 2009 (in Japanese).

Copyright Statement